Research Article

An Analysis of the Mechanical Characteristics and Constitutive Relation of Cemented Mercury Slag

Xinwei Li,[1,2] Sui Zhang,[1] E-chuan Yan,[2] Duoyou Shu,[1] Yangbing Cao,[3] Hui Li,[4] Siyang Wang,[1] and You He[1]

[1] Geological Party 103 Guizhou Bureau of Geology and Minerals, Tongren 554300, China
[2] China University of Geosciences, Wuhan 430074, China
[3] Fuzhou University, Fuzhou 350108, China
[4] Environmental Geological Prospecting Institute of Hebei Province, Shijiazhuang 050011, China

Correspondence should be addressed to Xinwei Li; lixinwei0510@163.com

This study focuses on mercury slag in the Tongren area of Guizhou Province, China. Computed tomography (CT) is used with uniaxial and triaxial compression tests to examine the mechanical changes in cemented mercury slag and its formation. The CT results for the uniaxial compression test reveal the overall failure process of the mercury slag structure. Based on the coarse-grained soil triaxial test, a modified Duncan-Chang model is compared with the actual monitoring results and is found to be suitable for the analysis of the slag constitutive model.

1. Introduction

China was one of the first countries to discover and exploit mercury resources. According to data collected in 2011, China has proven mercury reserves of 14.38×10^4 t and total reserves of 8.14×10^4 t. Guizhou Province accounts for more than 70% of the total reserves. China's largest mercury mine is within 30 km of Tongren City, Guizhou Province, and this mine's mercury production in the last century has ranked first worldwide. Thus, this resource is known as "China's mercury" [1–4].

Mercury is found in nature in relatively low quantities. The mercury content in ore must be greater than 0.8% to qualify as industrial grade. Thus, large amounts of mining waste and smelting tailings are produced during mercury mining. In early mining efforts, large quantities of slag waste were left untreated in the mining area near the free stack without awareness of the potential implications [5–8]. Over time, however, the accumulated formation of cemented mercury slag has led to concerns over its stability.

Mercury slag is similar to other slag materials in that it consists of slag or granular waste residue. The structure is loose, the water permeability is high, and the stability is generally poor. Under the action of an external disturbance or long-term environmental forces, slag debris flow occurs easily, which can lead to geological disasters (e.g., collapse and landslides) and mercury pollution of the environment. For example, the Donglin coal gangue hill of the Chongqing Nantong Mining Bureau collapsed on 25 October 2005, resulting in one person being buried. In another case, the gangue hill for an old house-based coal preparation plant of the Guizhou Panjiang Coal and Electricity Group Company experienced a major landslide on 16 April 2006 that buried seven people. The accumulation of large amounts of mercury slag adversely influences the mining landscape and environmental safety (leading to, e.g., rocky desertification, geological disasters, and environmental pollution). Therefore, the mechanical properties and constitutive relation of cemented mercury slag aggregates must be studied, and the stability of the slag accumulation body must be analyzed. Such studies are

important for ensuring the geological safety of a mining area and ensuring a relatively unpolluted living environment.

2. Research Status in China and Elsewhere

Because of the complexity and variability of the structure of cemented mercury slag, there have been few studies on the stability of slag accumulation. The mechanical properties and constitutive parameters of cemented mercury slag in the stacking state continue to be a source of controversy.

In the study of the crystallisation mechanism and cementation mode of cemented mercury slag, researchers have relied on methods developed to analyze other types of materials. For example, some researchers [9–14] have analyzed the basic mechanical properties and influence factors for natural-grade gravel material mixed with a small amount of cemented rock and found that cemented rock-fill has both the properties and characteristics of concrete. Chen et al. [15] analyzed the effect of soil structure, soil erosion, and moisture retention; the result indicated that the type of backfill soil affects the quality of the artificial soil significantly. Kara and Baykara [16] investigated the characteristics of three neighboring soils from the NE of Turkey and elucidated the effect of different land-use management on the soil aggregate stability and microbial biomass in Galyan-Atasu dam watershed. All these results showed that the supply and demand of nutrients to the soil in the samples are largely dependent on the type, quantity, and presence of the cemented substances. However, the lack of basic research on the structure of cemented mercury slag has limited the scientific management of such slag.

The lack of experimental research on the mechanical properties of cemented mercury slag has resulted in the absence of a constitutive model. The triaxial test is commonly used to study the mechanical properties of cemented soil materials [17], such as cemented carbide slag. Asghari et al. [18] simulated hydrated lime cement and performed a triaxial shear test on cemented coarse-grained soils from the Tehran suburbs. That group found that the cement strength plays a decisive role in the peak shear strength of cemented coarse-grained soils. Kongsukprasert et al. [19] conducted a series of triaxial shear tests on cemented gravel and found that the moisture content, strike strength, and mass ratio of cement ash to gravel have a significant effect on the stress-strain relationship.

Because of the lack of a constitutive model for cemented mercury slag, we are left to draw on the current classical constitutive relation based on the engineering characteristics and special requirements of cement residue and to perform repeated experiments to obtain a more practical cemented mercury slag constitutive model. Candidate classical constitutive models include the following: the Cambridge model, the Duncan-Chang hyperbolic nonlinear elastic model, the Lade-Duncan elastic-plastic model [20], Matsuoka and Nakai's spatial mobilised plane [21], the multiple yield surface model [22–25], and the nonlinear K-G model [26]. Because each constitutive model has its own scope of application and each material has its own complexity, corrections must be made to the models, depending on the conditions. For example, Jia et al. [27] proposed a modified Mohr-Coulomb model that considers the maximum tensile stress criterion to compensate for the limitations of the Mohr-Coulomb criterion when describing the tensile properties of a rock mass over a certain range. In Liu et al. [28], based on the "elastic modulus method" derived from the hypothesis of strain equivalence and test data of complete stress-strain curves of marble, granite, and sandstone under uniaxial compression, a damage model in the form of logistic equation is proposed to simulate the stress-strain relation of rocks. This model provides a method for estimating the elastic modulus of undamaged rocks using uniaxial compression test results and it presents a reasonable explanation of the chaos phenomenon occurring in uniaxial compression test. Saberi et al. [29] considered the particle breakage and proposed a constitutive modeling of gravelly soil-structure interface. Ma et al. [30] present a new approach for the development of an elastoplastic constitutive model to predict the strength and deformation behavior of soils under general stress conditions. Stutz and Mašín [31] proposed a new hypoplastic interface model and pointed out that this model can describe a number of important phenomena of clay-structure interfaces. Xiao and Liu [32] proposed an elastoplastic model considering state dependence and particle breakage and pointed out that the model considering particle breakage can well predict the stress-strain and particle-breakage behaviors of rock-fill materials at various confining pressures. Their model can simultaneously reflect the mechanisms of compressive and shear deformations. Because the physical properties of cemented mercury slag are similar to those of this soil and the stone materials, the research described above can be used to develop a constitutive relationship for cemented mercury slag.

Our literature review indicates that there has been no basic research on the structure, physical properties, mechanical properties, or constitutive relation of cemented slag in China or elsewhere. By referring to the research of other materials, however, the physical properties and constitutive relationship of the slag can be determined to analyze the stability of mercury slag landfills.

3. Methodology

Mercury slag in Tongren, Guizhou Province, was selected as the research object. First, computed tomography (CT) and uniaxial and triaxial compression tests were performed to study the mechanical changes to cemented mercury slag and its formation [33]. Second, based on a constitutive model of coarse-grained soil, a constitutive model of cemented mercury slag under typical conditions was developed. Finally, the constitutive model and Duncan-Chang model were applied to a stability simulation analysis of a representative cement-type mercury slag accumulation body and compared with the actual monitoring results of the mine to verify the rationality of the cemented slag constitutive model. The conclusions of this study and the technical methods used during the research process can provide basic theoretical support for managing mercury slag stability.

Table 1: Relative density test results (700 samples).

Years	Maximum dry density (g/cm^3)	Relative density of 0.75 dry density (g/cm^3)	Relative density of 0.80 dry density (g/cm^3)	Relative density of 0.85 dry density (g/cm^3)	Sample site density (g/cm^3)
40	2.275	1.706	1.820	1.933	1.721
70	2.358	1.769	1.886	2.004	1.794

Table 2: Particle size distributions (700 samples).

Particle size (mm)	60–40	40–20	20–10	10–5	5–2	2–1	1–0.5	0.5–0.25	0.25–0.1	<0.1	Total
40-year group											
Content (%)	10.8	23.6	31.6	14.5	4.0	2.7	2.0	3.5	3.0	4.3	100
70-year group											
Content (%)	5.4	27.1	30.9	15.6	4.0	2.9	2.3	3.6	3.5	4.7	100

3.1. Materials. The mercury slag in Tongren is composed primarily of waste slag, tailings, and soot. The physical and chemical properties of the slag are stable in its natural state, and the physical and mechanical properties of the slag are stable under natural conditions. The physical and mechanical properties of the slag increase with its mechanical strength. Tailings due to calcination can cause the material composition to change. This process can destabilise the chemical properties and cause a chemical reaction to occur. Tongren has a humid climate with frequent rain; the tailings can slag through the leachate to crystallise the cement. The cement flows with the leachate and fills the skeleton of the waste slag, tailings, and ashes to form a cement paste.

To consider the time effect on the cementation of mercury slag, 40- and 70-year aggregates of 700 mercury slag heaps were selected for field sampling. Table 1 presents the relative densities of the cemented mercury slag, and Table 2 presents the particle size distribution.

Due to cementation, the cohesion of the cemented mercury slag was enhanced, and a hardened "shell" appeared outside the accumulation body. An investigation on the instability of cemented mercury slag accumulation in Tongren found that the main failure mode was a failure at the slope toe, as shown in Figure 1. In fact, because of the protective effect of the hardened shell, the other three types of damage were also directly related to the slope. Therefore, it is of practical importance to study the common occurrence of cemented mercury slag, which plays a controlling role in the destruction of traceability.

Based on the similarity between cemented dross and gravel, cemented mercury slag with residual strength in the saturated state plays a decisive role in the stability of the deposited body and was found to be the most common cemented mercury slag in Tongren. In this study, this composition was taken to be the representative state of cemented mercury slag.

3.2. Description of the Experiment

3.2.1. Uniaxial Compression CT Test. Figure 2 shows the CT visualisation system of the Key Laboratory of Ministry of Water Resources of Chang'an Academy that was used for the indoor uniaxial compression CT test. Samples were collected from the initial state, preloading, loading, and failure stages of glial gravel grit mercury slag. The stress-strain relationship of the sample and the structural meso failure response process were analyzed. Table 3 presents the main technical parameters of the CT testing system (SOMATOM Sensation 40, Siemens).

The procedure for the uniaxial compression CT test was as follows.

(1) Sample Preparation. A handheld gasoline drill and standard sampler were used to take samples of 40- and 70-year cementation particles from a <30 mm layer of glial gravel grit mercury slag. The samples were 100 mm in diameter and 200 mm in length.

(2) Scanning before Experiment. Before the test, the samples of glial gypsum gelled mercury slag were measured, as shown in Figure 3(a). The test samples were installed in the triaxial instrument, as shown in Figure 3(b). A CT scan was performed to determine the initial state of the glial gravel grit mercury residue slag samples, as shown in Figure 3(c).

(3) Uniaxial Compression to Sample Failure. The samples were subjected to uniaxial compression until destruction while being monitored throughout the process, as shown in Figure 3(d). CT images of the same position at different time points were selected, and the mechanical structure of the damaged sample structure was analyzed.

3.2.2. Triaxial Compression Test of Coarse-Grained Soil. A large-scale triaxial test was performed on coarse-grained soil to simulate the failure of the specimen under multidimensional dynamic and static conditions and obtain the stress-strain relationship of cemented mercury slag. Table 4 presents the main technical parameters of the 2000 kN microcomputer-controlled electrohydraulic servo triaxial testing machine (Model TAJ-2000) of China's Geological University Zigui Practice Base Laboratory. This type
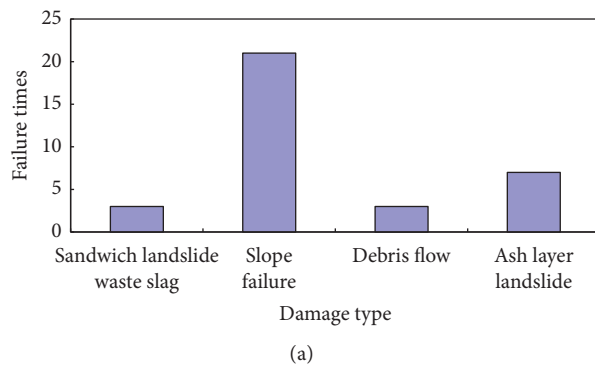
(a)

(b)

FIGURE 1: Investigation results for the main failure mode of mercury slag accumulation in the Tongren area: (a) types and (b) slope foot source damage.

TABLE 3: Main technical parameters of SOMATOM Sensation 40.

Project	Content
Aperture	70 cm
Tilt angle	±30°
Rack rotation speed	162 r/min
Detector	40 rows of rare earth ceramic (UFC) variable array detector (AAD) acquisition system
Number of detectors	26,880
Data collection system	40 layers; 1344 channels per layer, 4640 times per revolution projection
Tube	Electron beam control Straton tube
Tube heat capacity	0.6 MHU
Anode heat dissipation rate	5 MHU/min
High-voltage generator	70 kV
Voltage range	80, 100, 120, 140 kV
Tube current	28–580 mA

FIGURE 2: CT visualisation system.

of instrument is used primarily for coarse particles: axial pressure and lateral pressure strength tests of sands and soils and soil dynamics tests.

The test procedure was as follows.

(1) Sampling. 700 samples of 40- and 70-year accumulated mercury slag were produced using a portable drill and standard samplers with a length of 200 mm and a diameter of 100 mm. Each sample was formed by partitioning slag into eight pieces.

(2) Sample Preparation. The specimen height was set to 600 mm, and the diameter was set to 300 mm. The control dry density was 1.8 g/cm^3. The stratified compaction vibration method was used, as shown in Figures 4(a)–4(c). A vacuum was applied between the sample and rubber film to remove bubbles and ensure that the sample would not be damaged and that the gap would be reasonably filled, as shown in Figure 4(d). After a sample was installed, the head saturation method was used to bring the sample to the saturation point, as shown in Figure 4(e).

(3) Consolidation Drainage Test. After a sample was installed, gas was exhausted through the exhaust pipe. The initial water head was recorded, and the sample was examined to determine if it was fully saturated; if not, it was resaturated. Shear tests were performed on samples with confining pressures of 0.2, 0.4, 0.6, and 0.8 MPa. During the shear process, the strain rate was controlled, and the changes to the axial load
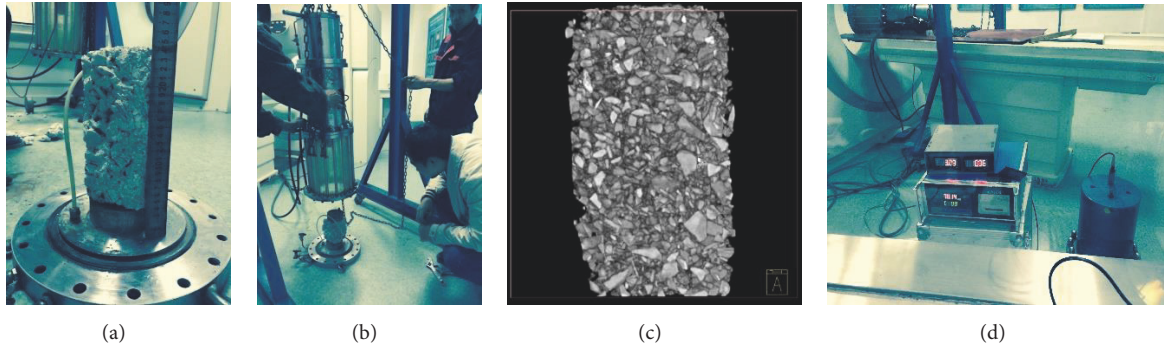
(a)   (b)   (c)   (d)

FIGURE 3: Steps of the uniaxial compression CT test: (a) sample, (b) sample installation, (c) test sample facade structure, and (d) data reading in the trial.

TABLE 4: TAJ large moving and static triaxial instrument.

Project	Main indicators
Test size	$\Phi 300\,mm \times 600\,mm$
Axial maximum test force	Static: 2000 kN, dynamic test range: 0–1000 kN
Axial displacement measurement range	0–300 mm
Confining system	Maximum confining pressure: 10 MPa; dynamic confining pressure: 0–3 MPa
Pore water pressure	0–10 MPa (accuracy: ±1% RO)
Vibration frequency	$F \geq 0.1$ Hz (full load: ±700 kN, displacement amplitude: ±70 mm) $F \leq 10$ Hz (full load: ±200 kN, displacement amplitude: ±1 mm)
Load form	Sine, triangular, square, and random waves; the impact load speed is greater than 10 mm/s
Control system	Can use stress and strain control, vertical and circumferential load synchronisation, or phase control

(a)   (b)   (c)

(d)   (e)   (f)

FIGURE 4: Triaxial compression test procedure: (a) mould tube installation, (b) sample weighing, (c) sample layer vibrating chamber, (d) sample vacuum forming, (e) sample saturation, and (f) sample shear failure.
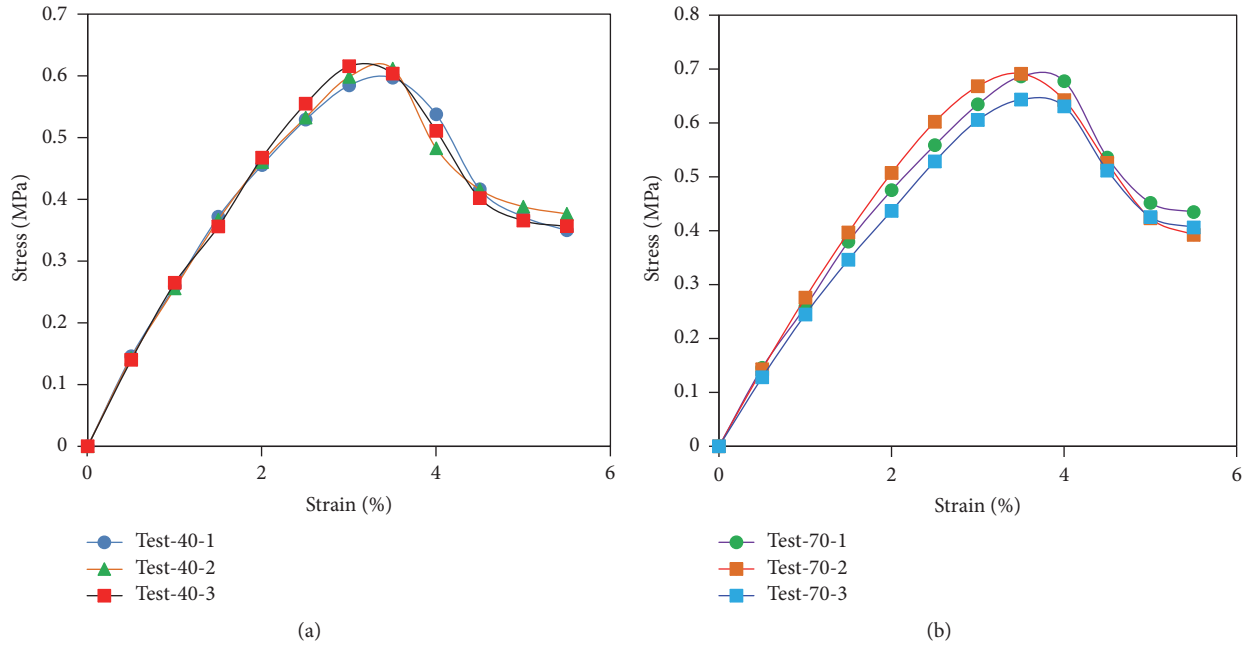
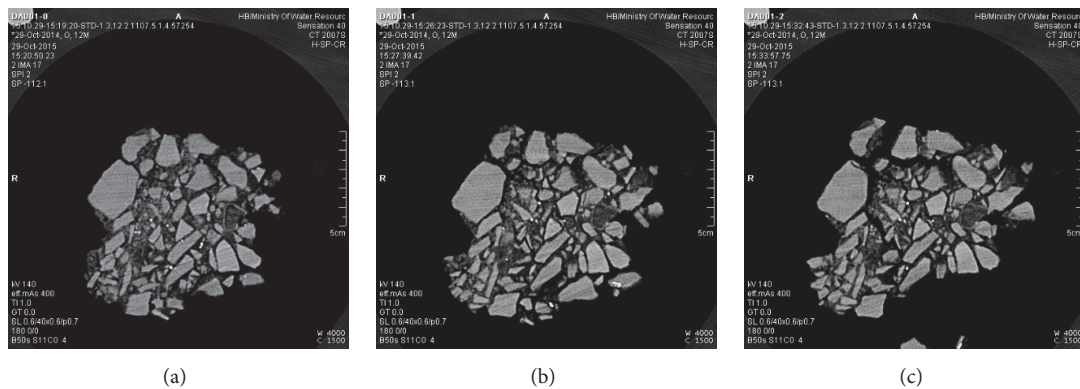FIGURE 5: Stress-strain curves for cemented mercury slag: (a) 40 years and (b) 70 years.

FIGURE 6: CT scan results for a cracked cross section of the 40-year sample at the same location for different compression times.

and volume were recorded at strain increments of 1 mm. The results are shown in Figure 4(f).

4. Results

4.1. Analysis of Uniaxial Compression Failure of Cemented Structures. Figure 5 shows the macroscopic stress-strain curves that were obtained from the uniaxial compression test on 40- and 70-year glial gravel gelled mercury slag raw materials. By analyzing the corresponding cross-sectional structure of each sample in the same position, as shown in Figures 6 and 7, the stress-strain response of the typical mercury slag structure was obtained.

(1) The stress-strain curve and CT scan showed that the internal cementation structure tended to be closed before the stress was relatively high. The strength increased with the stress, and the cemented mercury

slag was elastic in the initial stress-strain process. The stress-strain curve can be used to characterise the linear elastic behavior.

(2) When the stress concentration reached its peak, the cemented mercury slag structure presented a corresponding response. When the stress increased with the initial crack, the strain did not show any significant increase. The tangent stress curve was relatively flat, and the slope was small. At this point, the cemented mercury slag structure maintained the overall peak strain.

(3) As the stress increased, the structure of the cemented mercury slag was rapidly damaged. One overall and two local failure modes were observed. The overall failure and stress-strain curve corresponded to rapid expansion of the crack after unloading. When the force increased slightly, the crack expanded, as shown

(a)   (b)   (c)
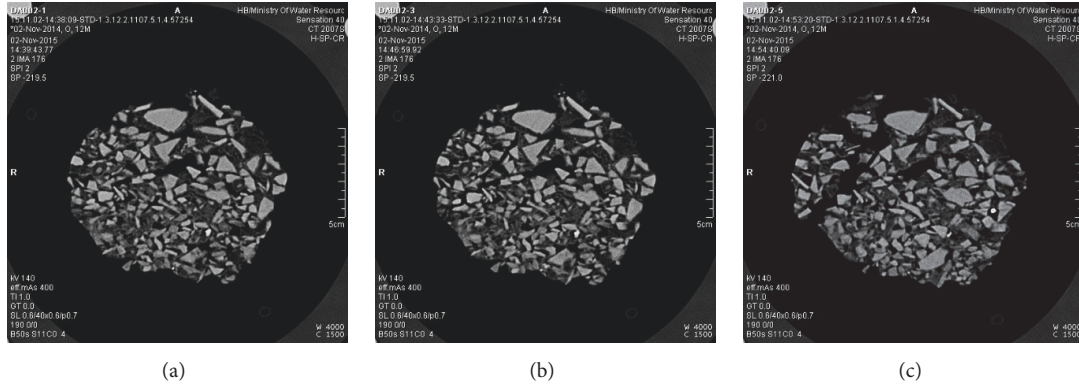
FIGURE 7: CT scan results for a cracked cross section of the 70-year sample at the same location for different compression times.

in Figures 6 and 7. The local damage was caused by the collapse of blocks at the edge or surface from cracks that led to separation from the main body.

(4) When the strain did not change with increasing stress, the mercury slag structure lost its response mechanism and was completely destroyed. At this time, the structure of the specimen was thoroughly penetrated, and the specimen was completely destroyed. The mechanical strength of the structure was terminated, as shown in Figure 7.

4.2. Analysis of the Strength Parameters of Cemented Mercury Slag under Typical Conditions. Cemented mercury slag typically has a granular structure that generally cannot bear tensile stress. More research is required on the shear strength characteristics of this slag. The relationship between the normal stress, shear stress, and shear strength on the failure surface under shear conditions is generally described as follows:

$$t_f = c + \sigma \tan \varphi. \tag{1}$$

Based on the maximum axial stress and confining pressure derived from the triaxial experiment, a Mohr circle can be drawn for the two sets of samples with $\sigma_1 + \sigma_3/2$ as the centre and $\sigma_1 - \sigma_3/2$ as the radius. The values of c and φ for the cemented mercury slag in the saturated state are obtained as shown in Figures 8(a) and 9(a). In the case of cemented mercury slag, which is similar to coarse-grained soil, the particle distribution with crushing occurs at a low confining pressure. At this point, the stress between particles is redistributed, and the connecting forces between the particles are weakened, resulting in lower friction. The strength of the envelope is not a straight line and presents a downward bending curve, as shown in Figures 8(b) and 9(b). The following equation is typically used to obtain φ_0, $\Delta \varphi$, and the relationship with the shear strength for the sample:

$$\varphi = \varphi_0 - \Delta \varphi \lg \frac{\sigma_3}{p_a}, \tag{2}$$

where p_a is the atmospheric pressure and φ_0 is the value of φ when $\sigma_3 = p_a$.

The contrast between the strength envelopes of the 40- and 70-year cemented slags can be interpreted using the Mohr-Coulomb strength criterion. The cemented mercury slag with 40 years of accumulation had lower bond strength than the slag with 70 years of accumulation and a lower friction angle. This result indicates that the consolidation stress of cemented mercury slag increases over a long duration, resulting in greater cohesion of the sample with longer stacking times. In addition, because the internal particles of the slag did not change, the internal friction angle did not greatly change. When plotted, (2) clearly shows the increase in the curve as accumulation occurs over a longer period. The consolidation stress further increases, and φ_0 shows a substantial increase. As the consolidation stress increases with the accumulation time, the particles inside the slag harden at a lower confining pressure. Thus, the slag becomes stronger and less prone to deformation.

5. Constitutive Model of Cemented Mercury Slag

Three notable coarse-grained soil constitutive models are the Rowe dilatancy model, the K-G model, and the Duncan-Chang model. The Rowe dilatancy model is based on the principle that the minimum interaction can be compared using energy principles; the interaction between pairs of particle is used to simulate the global interaction between all particles. This model can capture the deformation of coarse grains; however, the impact of particle crushing is not considered, and limitations remain. For the K-G model, the expression is relatively simple: the stress and strain are decomposed into a dilatational (or hydrostatic) tensor and a deviatoric tensor, where the dilatational stress tensor corresponds to the dilatational strain tensor and the deviatoric stress tensor corresponds to the deviatoric strain tensor. The Duncan-Chang model, which is also called the hyperbolic model, is a type of subelastic model that employs a nonlinear elastic constitutive relation. It is straightforward to determine the parameter values through experiment. The formula is simple, the concept is clear, and much engineering application experience has been accumulated using this formula.
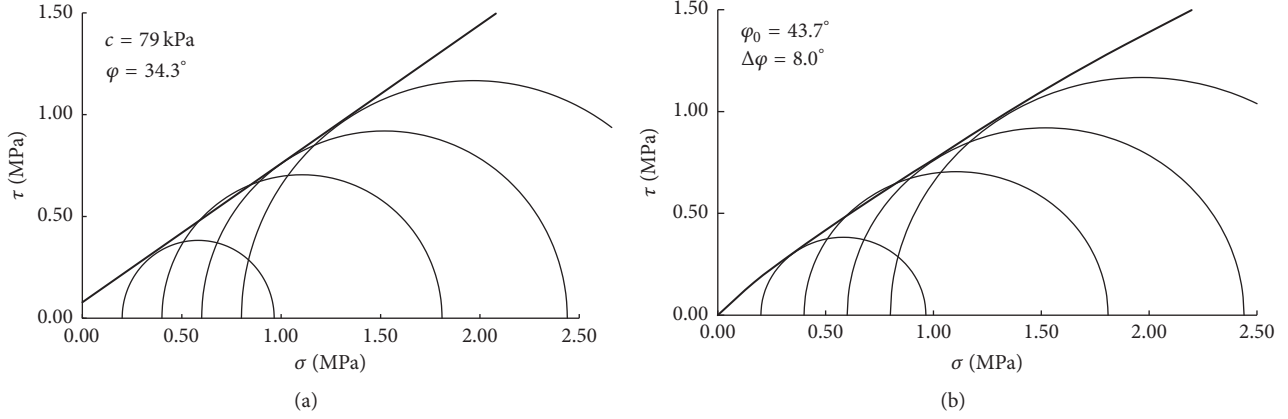
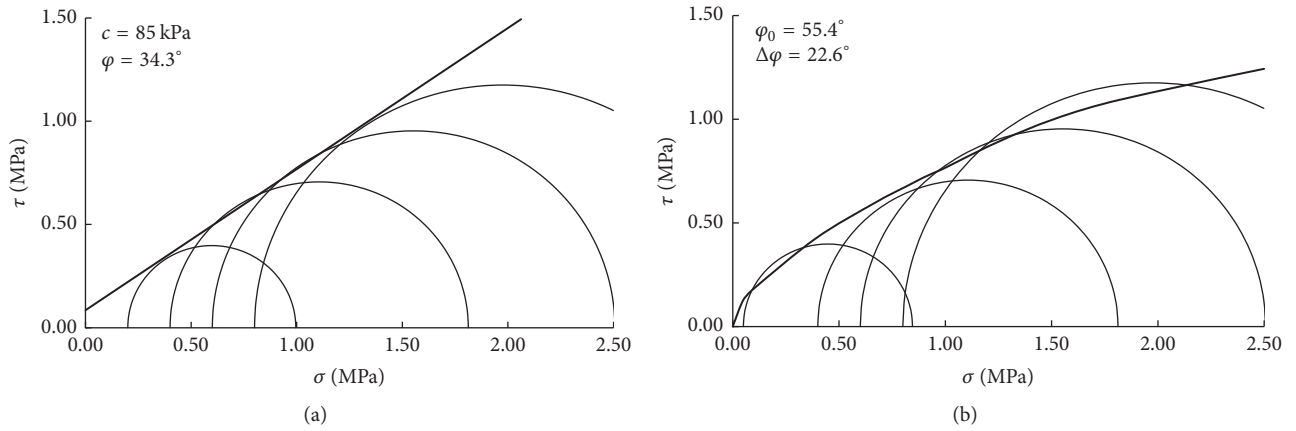FIGURE 8: Shear strength envelope of the 40-year cemented mercury slag.

FIGURE 9: Strength envelope of the 70-year cemented mercury slag.

Cement-type slag is predominantly coarse-grained, and the stress-strain relationship is similar to that of coarse-grained soil. The Duncan-Chang constitutive model was used in this study. Based on an analysis of the experimental data, the ε_1-ε_3 relationship was improved, and an expression for Poisson's ratio ν_t was derived to obtain an improved Duncan-Chang (E-ν) constitutive model.

A triaxial compression test was conducted on the 40- and 70-year mercury slag samples. The test results were used to improve the ε_1-ε_3 relationship and establish the constitutive model.

5.1. Improved Characterisation of the ε_1-ε_3 Relationship. According to the conventional triaxial test results, as shown in Figures 10(a) and 10(b), the main stress difference $(\sigma_1 - \sigma_3)$ increased with the axial strain ε_1 before finally stabilising, but the volume strain continued to increase. If the axial strain ε_3 is defined as positive, then the ε_1-ε_3 relationships with pressure are as shown in Figure 11.

Data analysis indicated a parabolic relationship between ε_1 and ε_3 set at the origin. Based on this finding, the relationship between the two was set to

$$\varepsilon_1{}^2 = A\varepsilon_3{}^2 + B\varepsilon_3, \tag{3}$$

TABLE 5: A and B values under different confining pressures.

Confining pressure (MPa)	0.2	0.4	0.6	0.8
A	3.7474	3.2756	3.4282	3.1515
B	0.2662	0.4427	0.4948	0.7257

where A and B are test parameters for which a fitting curve is available through data analysis, ε_1 is the axial strain, ε_3 is the lateral strain, and $\varepsilon_1{}^2$ and ε_3 are fitting results (specified in Table 5) for a parabolic relationship.

According to Table 5, the value of A for a sample under different confining pressures changes only minimally. Thus, the average value of A under all tested confining pressures can be used. The value of B increases with the confining pressure, and the growth rate gradually decreases. Through data analysis, B and $\lg(\sigma_3/p_a)$ are established to have the following linear relationship:

$$B = t_1 \lg\left(\frac{\sigma_3}{p_a}\right) + t_0, \tag{4}$$

where t_0 and t_1 are test constants obtained by linear fitting, p_a is the standard atmospheric pressure, and σ_3 is the test confining pressure.
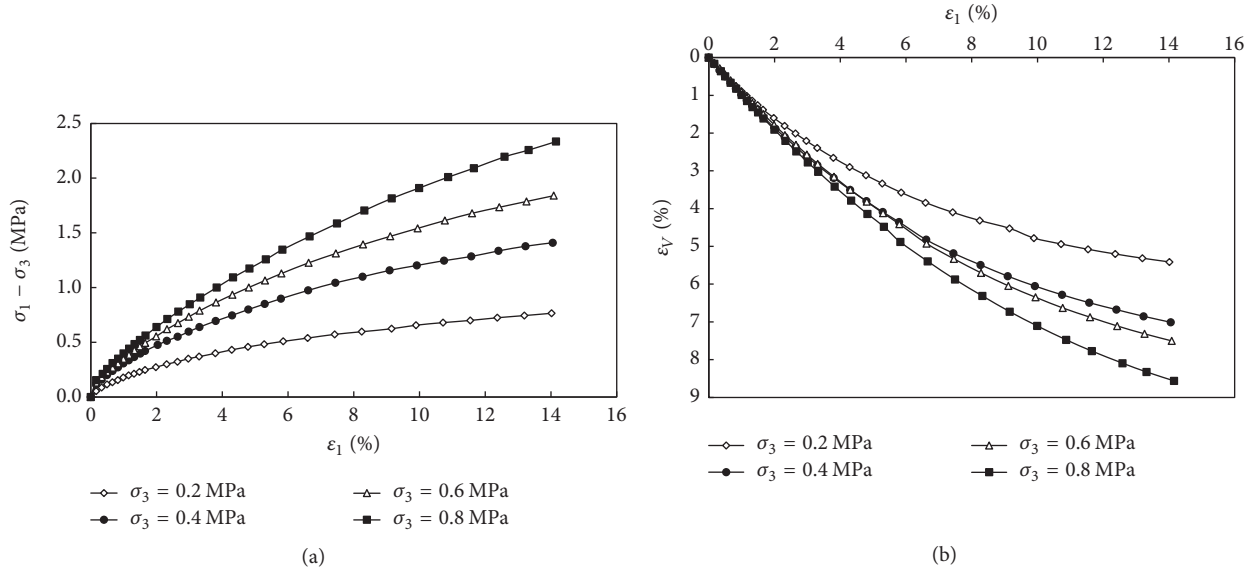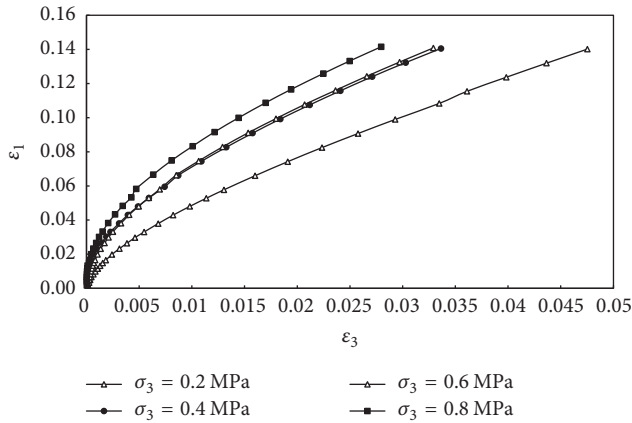
(a)

(b)

FIGURE 10: The conventional triaxial test results.

FIGURE 11: Sample relationship curves of ε_1-ε_3.

TABLE 6: Measured results for the fitted parameters.

Parameter	A	t_1	t_0
Value	3.4007	0.6873	0.0384

$$= \frac{\varepsilon_1}{\sqrt{A\varepsilon_1{}^2 + 0.25\left[t_1 \lg\left(\sigma_3/p_a\right) + t_0\right]^2}}. \tag{7}$$

Table 6 presents the fitting parameter values based on the sample results.

The value of ν_t predicted using (7) agrees with the measured value, as shown in Figure 13. This finding indicates that the fitted parameter values are reasonable.

Relative to the original Poisson ratio in the original E-K model, the initial Poisson ratio was 0, primarily because the sample started to compress. As the pores of the specimen became closed, the deformation of the pores after lateral deformation was the main source of the initial axial deformation. Therefore, the initial Poisson ratio is more consistent with the test phenomenon. At different confining pressures, the tangential Poisson ratio tended to stabilise with increasing axial strain. For the experimental specimen, the final sample deformation and tangential Poisson's ratio stabilised with increasing axial stress. For the test sample, as the axial stress increased, the final sample deformation and tangential Poisson's ratio stabilised. The improved Poisson ratio was consistent with the experimental results. Therefore, the improved Duncan-Chang model better reflects the stress-strain relationship of cemented mercury slag under typical conditions.

6. Simulation for the Stability of Cemented Mercury Slag

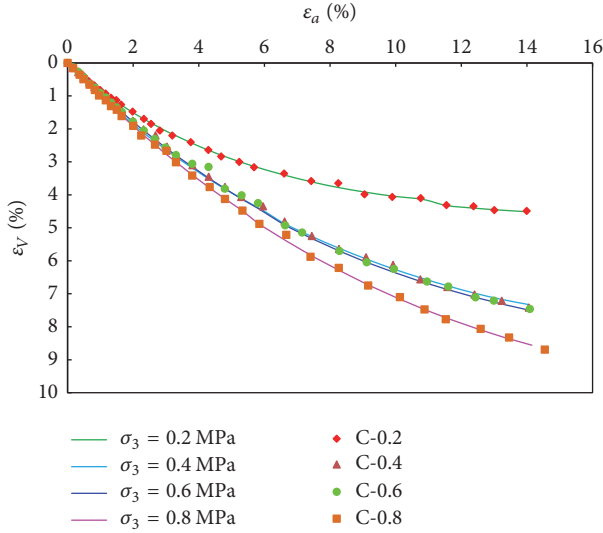The Duncan-Chang E-ν model was transformed into the incremental expression required for secondary development

5.2. Discussion of Volume Strain ε_v.

ε_v is defined as follows:

$$\varepsilon_v = \varepsilon_1 + \varepsilon_2 + \varepsilon_3 = \varepsilon_1 + 2\varepsilon_3. \tag{5}$$

By combining (3) and (5), the following relationship is derived:

$$\varepsilon_v = \varepsilon_1 + \frac{\left(B - \sqrt{B^2 + 4A\varepsilon_1{}^2}\right)}{A}. \tag{6}$$

Figure 12 compares the calculated (scatter) and measured (solid line) values for ε_v. The improved model matches the measured data well and reflects the volume strain of the cemented mercury slag under typical conditions.

5.3. Discussion of Poisson's Ratio ν_t.

According to (3), ν_t can be expressed as follows:

$$\nu_t = \frac{d\varepsilon_3}{d\varepsilon_1} = \frac{\varepsilon_1}{\sqrt{A\varepsilon_1{}^2 + 0.25B^2}}$$

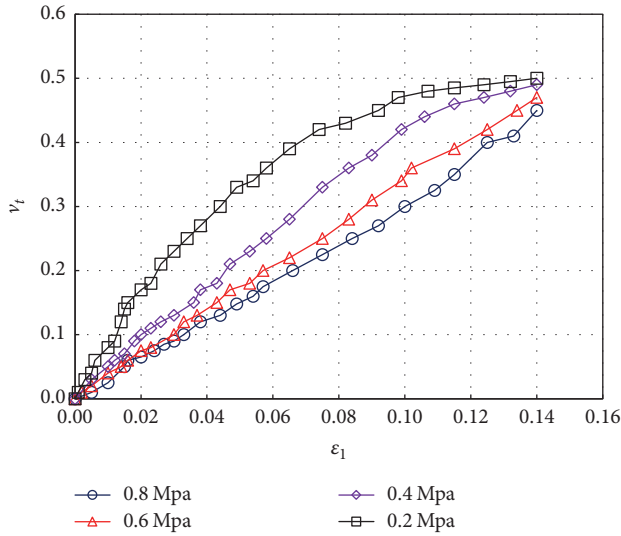FIGURE 12: Measured and calculated ε_v values.

FIGURE 13: Chart comparing the measured and predicted v_t values.

of the FLAC^{3D} constitutive relation. The constitutive model library of FLAC^{3D} was used in this process. The improved Duncan-Chang constitutive model was applied to numerical analysis of the slope of a mercury slag accumulation body and compared with the actual deformation and failure process of the slope to further verify the correctness and applicability of the model.

6.1. Overview of Project Examples. The type of cemented mercury slag of interest was formed over approximately 30

years. The maximum elevation of the top of the slag was 873.00 m. The length of the deposited body was approximately 50.0 m, the width was approximately 35.0 m, the measured plane area was approximately 1476.3 m^2, and the volume was approximately 2657.3 m^3. Thus, the body was considered a small slag accumulation body.

The Duncan-Chang model can be used to describe the stress-strain characteristics of cemented mercury slag in the accumulation body, which is characterised by a loose slag structure, high porosity, and low mechanical strength. The thickness of the bulk layer was 0.2–2.5 m with an average thickness of 1.8 m. The thickness decreased from the slope top to the foot. The bedrock was 106° ∠ 20°, and the thickness was 216–386 m. Figure 14 shows the section structure.

6.2. Mechanical Parameters of Bedrock. The indoor test results show that the upper part of the accumulated slag had a density of 1560 kg/m^3, an apparent density (basket method) of 2828 kg/m^3, and a porosity of 44.8%. Based on the high porosity of the deposit, the natural gravity of the slag accumulation body is expected to be 16.70–18.5 kN/m^3. Based on the engineering geology analogy method and local rock and soil surveying experience, the physical and mechanical parameters of the bedrock in the field are as given in Table 7 according to the *Basic Code for Building Foundation Design* (GB500007-2002).

6.3. Incremental Expression for the Constitutive Relation. FLAC^{3D} uses an incremental constitutive relation; the stress increment is calculated from the strain increment, and the total stress is obtained by superimposing the stress calculated in the previous period. According to FLAC^{3D}'s own UDM custom constitutive documents in the stensor.h header file, the stress tensor structure StnS export function EXPORT bool *Resoltopris ()* can be the current unit stress field along the three principal axes.

In this study, the FLAC^{3D} constitutive model was developed using the E_t-v_t model; the modified Duncan-Chang E_t-v_t replaces the stress sign:

$$E_t = K p_a \left(\frac{-\sigma_1}{p_a} \right)^n \left[1 - R_f \frac{(1 - \sin \varphi)(\sigma_3 - \sigma_1)}{2c \cos \varphi - 2\sigma_1 \sin \varphi} \right]^2,$$

$$v_t = \frac{\varepsilon_1}{\sqrt{A\varepsilon_1^2 + 0.25 \left[t_1 \lg (-\sigma_1/p_a) + t_0 \right]^2}}. \tag{8}$$

ε_1 can be used to derive the tangent elastic modulus E_t:

$$\varepsilon_1 = \frac{(\sigma_3 - \sigma_1)}{K p_a (-\sigma_1/p_a)^n \left[1 - R_f \left((1 - \sin \varphi)(\sigma_3 - \sigma_1)/(2c \cos \varphi - 2\sigma_1 \sin \varphi) \right) \right]}. \tag{9}$$
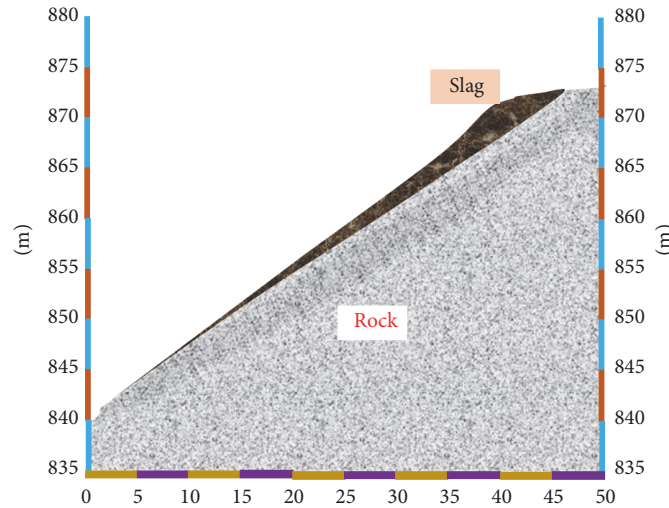
FIGURE 14: Stratigraphic profile.

TABLE 7: Physical and mechanical parameters of the bedrock.

Natural gravity (kN/m^3)	Poisson's ratio	Elastic modulus (GPa)	Cohesion (MPa)	Internal friction angle (°)	Tensile strength (MPa)
26.50	0.35	5.0	9.0	27	1.2

6.4. FLAC^{3D} Modeling. According to the slope shown in Figure 14 to establish the FLAC^{3D} calculation model, the vertical scale for the change in the slope of the terrain was not large. Thus, a plane model was used. The left and right boundaries were fixed to have an x-direction displacement of 0, and the bottom boundary had a z-direction displacement of 0. Because a plane model was used, the entire model had a y-direction displacement of 0. In terms of regional tectonics, the field is located at the junction of the Yangtze platform and South China fold belt. The regional folds are the Kyrgyzstan–Yuzhan oblique and Feng–Akira anticline, and the twofold axes are parallel to the northeast direction and lie 12 km apart. The impact on the construction of this area is small; thus, the model considered only the gravity field.

For the comparative study, the improved and unmodified Duncan-Chang E-ν models were used to improve the constitutive model parameters presented in Tables 8 and 9 under the boundary conditions for the bulk body model and gravity field. Table 8 presents the constitutive model parameters. Considering that the stacking age of this sample was approximately 30 years, Table 8 presents the selected model parameters. Table 9 presents the corresponding model parameters for a sample with a stacking age of 40 years. The simulation results were saved every 10,000 h. In total, 30,000 h were simulated.

6.5. Analysis of the Results. Figures 14 and 16 show the maximum horizontal displacement cloud and maximum shear strain cloud, respectively. As shown in Figures 15(a), 15(c), and 15(e), when the improved constitutive model was used on the slag, the maximum horizontal displacement of the accumulation body was concentrated predominantly near the foot. The slope of the surface had a relatively small range of change as the simulation steps increased. The body showed gradual upward expansion, which is consistent with the deformation process. Because no actual displacement monitoring data were available, the results could not be compared with the displacement values. Because of the influence of errors in the parameters, the simulated displacement value is not necessarily accurate but can fully reflect the deformation and evolution law. As shown in Figures 15(b), 15(d), and 15(f), the maximum horizontal displacement of the accumulation slope was concentrated at the top of the slope when the unmodified constitutive model was used.

As shown in Figures 16(a), 16(c), and 16(e), the maximum shear strain of the deposited body was concentrated primarily near the foot of the slope, and the initial small range of the slope surface increased with the simulation step. Figures 16(b), 16(d), and 16(f) show that the maximum shear strain was largest at the slope position of the deposited body. As the simulation time steps increased, the maximum shear strain was distributed predominantly in the rock near the contact surface rather than the slope surface. To further quantify the data, the modified model was used to simulate the deformation process in comparison with the actual monitoring results, as shown in Figure 17.

As shown in Figure 17, the horizontal displacements of the monitoring points at the same time step were in the order of A > B > C > D > E. Point A was located at the foot and had the largest displacement when the model simulation began, followed by points B, C, D, and E. The gradual increase in the slope surface displacement reflects the deformation process.

As described above, the Duncan-Chang E-ν model can be used to simulate the plastic deformation of a deposited body.

TABLE 8: Et-νt model parameters.

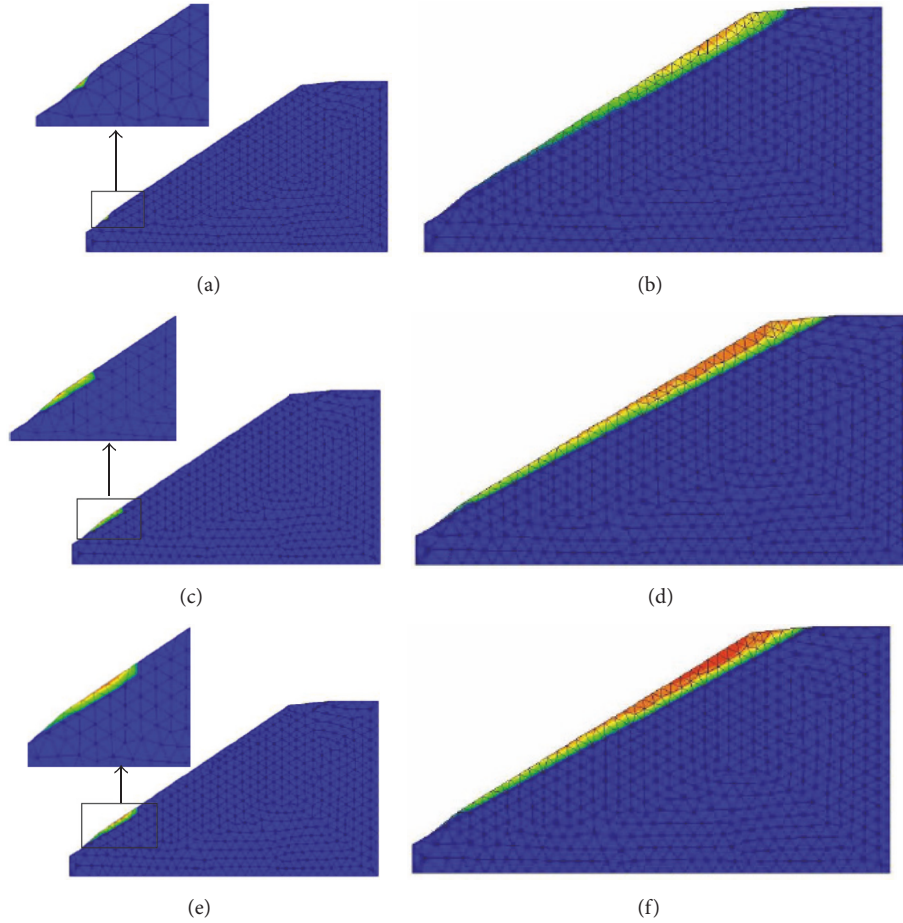| Years	Shear strength index				Et-νt model parameters							
	C' (kPa)	φ (°)	Φ_0 (°)	$\Delta\varphi$ (°)	K	n	K_b	m	R_f	G	F	D
40	78.6	34.28	43.75	7.99	150	0.538	29.9	0.51	0.744	0.088	0.063	6.88
70	85.1	34.33	55.36	22.55	332	0.141	55.5	0.13	0.774	0.089	0.074	6.93

(a)

(b)

(c)

(d)

(e)

(f)

FIGURE 15: Maximum horizontal displacements of the deposited body: improved model after (a) 10,000, (c) 20,000, and (e) 30,000 time steps; unmodified model after (b) 10,000, (d) 20,000, and (f) 30,000 time steps.

TABLE 9: Parameters for improving tangential Poisson's ratio in the Et-νt model.

A	t_1	t_0
3.4007	0.6873	0.0384

Moreover, the modified Duncan-Chang E-ν constitutive model can be used to study the displacement and shear strain to analyze the evolutionary process of deformation. When the unmodified Duncan-Chang E-ν constitutive model was used, the simulated cumulative slope deformation and evolution process did not match the actual slope deformation and failure phenomenon. This finding establishes that the modified Duncan-Chang E-ν constitutive model can reflect the actual situation better than the unmodified Duncan-Chang

E-ν constitutive model and that the improved constitutive model is not only correct but also meaningful.

7. Conclusion

This study focused on the stability of the slag accumulation body in the Tongren area of Guizhou Province, China. CT was used with uniaxial and triaxial compression tests to examine the mechanical properties and constitutive relation of cemented mercury slag aggregates. The main findings of this study are as follows.

(a) The stress-strain structural response of cemented mercury slag can be divided into four aspects. The internal cementation structure tends to be closed before stress exposure. When the stress concentration reaches its peak, the
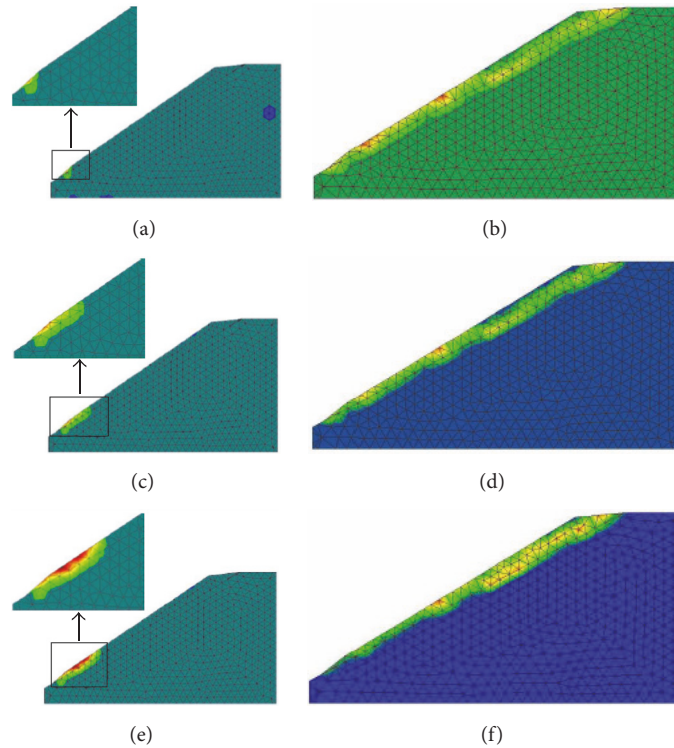
FIGURE 16: Maximum shear strain clouds of the deposited body: improved model after (a) 10,000, (c) 20,000, and (e) 30,000 time steps; unmodified model after (b) 10,000, (d) 20,000, and (f) 30,000 time steps.
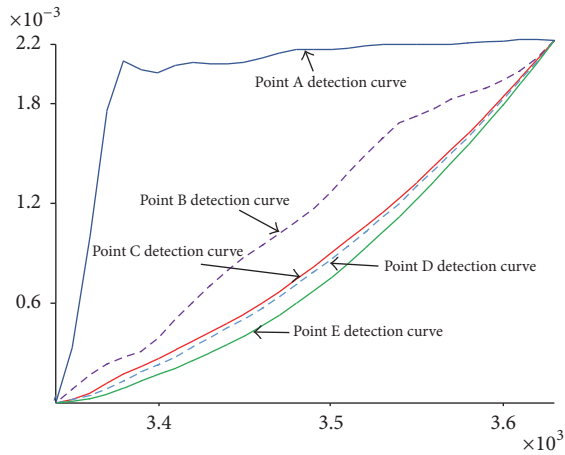

FIGURE 17: Measured horizontal shift of monitoring points.

structure of the cemented mercury slag presents the corresponding initial crack response. As the stress increases, the structure of the cemented mercury slag is rapidly damaged and exhibits one global and two local failure modes. When the strain does not change with increasing stress, the structure is completely destroyed, and the response of the mercury slag structure terminates.

(b) As the consolidation stress increases with the accumulation time, the particles inside the slag exhibit a hardening characteristic at lower confining pressures. This process makes the slag stronger and less prone to deformation.

(c) The modified Duncan-Chang E-v constitutive model is more likely to reflect the actual situation than the unmodified classic Duncan-Chang E-v constitutive model. This finding establishes that the improvement to the constitutive model is not only correct but also meaningful.

The results of this study are important for ensuring the geological safety of a mining area and establishing a nontoxic living environment. Future research may focus on the influencing mechanism of the grain roughness of mercury slag on the degree of consolidation.

Conflicts of Interest

The authors declare that there are no conflicts of interest regarding the publication of this paper.

Acknowledgments

References

[1] X. Liu, "Experimental Study on Mechanical Properties of Slag," *Yangtze River Sci. Res. Inst*, vol. 11, no. 4, pp. 46–51, 1994 (Chinese).

[2] Z. Wang, H. Lan, and J. Wu, "Present situation of Chinas raw mercury industry and suggestions for future shutdown policy," *Earth Environ*, vol. 42, no. 5, pp. 659–662, 2014 (Chinese).

[3] H. Yang, L. Ping I, and G. Qiu L, "Mercury pollution in mercury mining areas throughout the world: an overview," *Earth & Environment*, 2009 (Chinese).

[4] X. Feng, G. Li, and G. Qiu, "A preliminary study on mercury contamination to the environment from artisanal zinc smelting using indigenous methods in Hezhang County, Guizhou, China: Part 2. Mercury contaminations to soil and crop," *Science of the Total Environment*, vol. 368, no. 1, pp. 47–55, 2006.

[5] M. Horvat, J. Kotnik, M. Logar, V. Fajon, T. Zvonarić, and N. Pirrone, "Speciation of mercury in surface and deep-sea waters in the Mediterranean Sea," *Atmospheric Environment*, vol. 37, no. 1, pp. S93–S108, 2003.

[6] G. Qiu, X. Feng, S. Wang, X. Fu, and L. Shang, "Mercury distribution and speciation in water and fish from abandoned Hg mines in Wanshan, Guizhou province, China," *Science of the Total Environment*, vol. 407, no. 18, pp. 5162–5168, 2009.

[7] M. Fillion, D. Mergler, C. J. Sousa Passos, F. Larribe, M. Lemire, and J. R. D. Guimarães, "A preliminary study of mercury exposure and blood pressure in the Brazilian Amazon," *Environmental Health: A Global Access Science Source*, vol. 5, article no. 29, 2006.

[8] S. Wang, X. Feng, and G. Qiu, "The study of mercury exchange rate between air and soil surface in Hongfeng reservoir region, Guizhou, PR China," *Journal De Physique IV*, vol. 107, no. 1, pp. 1357–1360, 2003.

[9] M. E. Hines, M. Horvat, J. Faganeli et al., "Mercury biogeochemistry in the Idrija River, Slovenia, from above the mine into the Gulf of Trieste," *Environmental Research*, vol. 83, no. 2, pp. 129–139, 2000.

[10] Y.-N. Zhang and Y.-L. Chen, "Mechanical characteristics of cemented rockfill materials with high rock block proportions under uniaxial compression," *Journal of Northeastern University*, vol. 37, no. 11, pp. 1630–1634, 2016.

[11] Q. Zheng, C. Wang, and J. Zhang, "The strength and stress-strain behavior of the cemented rockfill," *Advanced Materials Research*, vol. 598, pp. 565–568, 2012.

[12] A. Fakhimi and B. Hemami, "Axial splitting of rocks under uniaxial compression," *International Journal of Rock Mechanics and Mining Sciences*, vol. 79, pp. 124–134, 2015.

[13] S. Zhang, H. Tang, H. Zhan, G. Lei, and H. Cheng, "Investigation of scale effect of numerical unconfined compression strengths of virtual colluvial-deluvial soil-rock mixture," *International Journal of Rock Mechanics and Mining Sciences*, vol. 77, pp. 208–219, 2015.

[14] A. Kesimal, E. Yilmaz, B. Ercikdi, I. Alp, and H. Deveci, "Effect of properties of tailings and binder on the short-and long-term strength and stability of cemented paste backfill," *Materials Letters*, vol. 59, no. 28, pp. 3703–3709, 2005.

[15] Z. Chen, R. Luo, Z. Huang et al., "Effects of different backfill soils on artificial soil quality for cut slope revegetation: Soil structure, soil erosion, moisture retention and soil C stock," *Ecological Engineering*, vol. 83, pp. 5–12, 2015.

[16] O. Kara and M. Baykara, "Changes in soil microbial biomass and aggregate stability under different land uses in the northeastern Turkey," *Environmental Modeling & Assessment*, vol. 186, no. 6, pp. 3801–3808, 2014.

[17] X.-W. Fang, Z.-H. Chen, C.-N. Shen, S.-G. Sun, and Q.-M. Wang, "Test study on residual soil under special stress paths," *Rock and Soil Mechanics*, vol. 26, no. 6, pp. 932–936, 2005.

[18] E. Asghari, D. G. Toll, and S. M. Haeri, "Triaxial behaviour of a cemented gravely sand, Tehran alluvium," *Geotechnical and Geological Engineering*, vol. 21, no. 1, pp. 1–28, 2003.

[19] L. Kongsukprasert, F. Tatsuoka, and M. Tateyama, "Several factors affecting the strength and deformation characteristics of cement-mixed gravel," *Soils and Foundations*, vol. 45, no. 3, pp. 107–124, 2005.

[20] J. M. Duncan and C. Y. Chang, "Nonlinear analysis of stress and strain in soils," *ASCE Soil Mech. Found. Div. J*, vol. 96, no. 5, pp. 1629–1653, 1970.

[21] H. Matsuoka and T. Nakai, "Stressstrain relationship of soil based on the SMP in," in *Proceedings of the 9th International Conference on Soil Mechanics and Foundation Engineering, Special Session*, vol. 9, pp. 153–162, London, UK, 1977.

[22] K. S. Choi and J. Pan, "A generalized anisotropic hardening rule based on the Mroz multi-yield-surface model for pressure insensitive and sensitive materials," *International Journal of Plasticity*, vol. 25, no. 7, pp. 1325–1358, 2009.

[23] W. Hu, "A novel quadratic yield model to describe the feature of multi-yield-surface of rolled sheet metals," *International Journal of Plasticity*, vol. 23, no. 12, pp. 2004–2028, 2007.

[24] H. L. Fang, H. Zheng, and J. Zheng, "Micromechanics-based multimechanism bounding surface model for sands," *International Journal of Plasticity*, vol. 90, pp. 242–266, 2017.

[25] R. L. Jackson and J. L. Streator, "A multi-scale model for contact between rough surfaces," *Wear*, vol. 261, no. 11-12, pp. 1337–1347, 2006.

[26] G. Li, *Discussion on three-dimensional constitutive relation of soil and model verification*, Tsinghua University, Beijing, China, 1985 (Chinese).

[27] S.-P. Jia, W.-Z. Chen, J.-P. Yang, and P.-S. Chen, "An elastoplastic constitutive model based on modified Mohr-Coulomb criterion and its numerical implementation," *Rock and Soil Mechanics*, vol. 31, no. 7, pp. 2051–2058, 2010.

[28] D. Liu, M. He, and M. Cai, "A damage model for modeling the complete stress–strain relations of brittle rocks under uniaxial compression," *International Journal of Damage Mechanics*, 2017, 105678951772080.

[29] M. Saberi, C. Annan, and J. Konrad, "Constitutive Modeling of Gravelly Soil–Structure Interface Considering Particle Breakage," *Journal of Engineering Mechanics*, vol. 143, no. 8, p. 04017044, 2017.

[30] C. Ma, D. Lu, X. Du, and A. Zhou, "Developing a 3D elastoplastic constitutive model for soils: A new approach based on characteristic stress," *Computers & Geosciences*, vol. 86, pp. 129–140, 2017.

[31] H. Stutz and D. Mašín, "Hypoplastic interface models for fine-grained soils," *International Journal for Numerical and Analytical Methods in Geomechanics*, vol. 41, no. 2, pp. 284–303, 2017.

[32] Y. Xiao and H. Liu, "Elastoplastic constitutive model for rockfill materials considering particle breakage," *International Journal of Geomechanics*, vol. 17, no. 1, pp. 1–13, 2017.

[33] X. W. Li, *Study on Mechanical Properties and Constitutive Relation of Cemented Mercury Slag*, China University of Geosciences, 2016.